

# Magnetically Actuated Dynamic Iridescence Inspired by the Neon Tetra

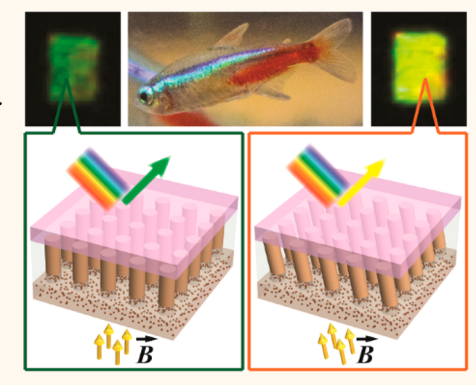
Zhiren Luo, <sup>†</sup>

Benjamin Aaron Evans, <sup>‡</sup> and Chih-Hao Chang\*, <sup>†</sup>

Description of the control of the control

Supporting Information

ABSTRACT: Inspired by the tropical fish neon tetra, we report a mechanism to achieve dynamic iridescence that can be magnetically tuned. This approach is based on the tilting of periodic photonic nanostructures, as opposed to the more common strain-induced color tuning. In this method, a periodic array of magnetic nanopillars serves as a template to guide the assembly of iron oxide nanoparticles when magnetized in a liquid environment. The periodic local fields induced by the magnetic template anchor the assembled particle columns, allowing the structure to tilt about the base when the angle of the applied field is changed. This effect emulates a microscopic "Venetian blind" and results in dynamic optical properties through structural coloration that is tunable in real time. The fabricated prototype demonstrates tunable reflectance spectra with peak wavelength shift from 528 to 720 nm. The magnetic actuation mechanism is reversible and has a fast response time around 0.3 s. This structure can be implemented on an arbitrary surface as



dynamic camouflage, iridescent display, and tunable photonic elements, as well as in other applications such as active fluidic devices and particle manipulation.

KEYWORDS: dynamic iridescence, neon tetra, structural coloration, ferrofluid, magnetic nanoparticles

t is widely known that organisms in nature can display spectacular colors. The coloration is primarily based on two mechanisms: pigmentary coloration ascribed to chemical dyes that absorb light within a narrow wavelength band, and structural coloration caused by the interference of visible light in periodic micro- and/or nanostructures, 1,2 or a combination of the two. Pigmentation is more prevalent and can be dynamic, such as the melanophores found in Atlantic salmon (Salmo salar),<sup>3</sup> but might suffer from photochemical degradation.1 On the other hand, structural coloration can have brilliant colors and tunable properties by real-time alteration of structure geometry such as the iridophores found in neon tetras (Paracheirodon innesi).<sup>4,5</sup> Furthermore, these two mechanisms can also work together for dynamic color, such as those observed in Atlantic salmon (Salmo salar) and panther chameleons (Furcifer pardalis). Structural colorations have been identified in a number of structures that are found in nature, including photonic crystals, <sup>7,8</sup> diffraction gratings, <sup>2,9</sup> and spiral coils. <sup>10</sup> These structural colorations can create either iridescent behaviors, where the colors gradually change as incident or viewing angles are varied, or noniridescent behaviors, where certain colors are reflected evenly at broad viewing angles. Two prominent examples of iridescent and noniridescent photonic crystals can be found in features of green peacocks (Pavo muticus)<sup>2</sup> and blue-and-yellow macaws (Ara ararauna, Psittacidae),<sup>8</sup> respectively.

Going beyond photonic structure with static coloration, some structures exhibit dynamic color changes that are responsive to stimuli. These structures can be utilized for camouflage that adjusts to different environments, 1,10 visual communication for aposematics 10 and mating, 10,11 and hidden signals that can be detected by polarization-sensitive organisms of conspecifics but not by predators. 10,11 To achieve dynamic color change, especially dynamic iridescence, lattice spacing of periodic nanostructures can be varied to alter the interference conditions. 1,12,13 This is also known as the "accordion" mechanism,4 where the lattice constant is mechanically strained by swelling or shrinking. This mechanism can be applied to one-dimensional (1D) multilayer platelets, twodimensional (2D) rod arrays, and three-dimensional (3D) crystals. It should be noted that the 1D, 2D, and 3D here refer to the periodicity of the structures. These 1D structures can be found in the squid (Loligo pealeii),14 the paradise whiptail ( Pentapodus paradiseus), 15 and the blue damselfish (Chrysiptera

Received: January 29, 2019 Accepted: March 19, 2019 Published: March 19, 2019



<sup>&</sup>lt;sup>†</sup>Department of Mechanical and Aerospace Engineering, North Carolina State University, Raleigh, North Carolina 27695, United

<sup>&</sup>lt;sup>‡</sup>Department of Physics, Elon University, Elon, North Carolina 27244, United States

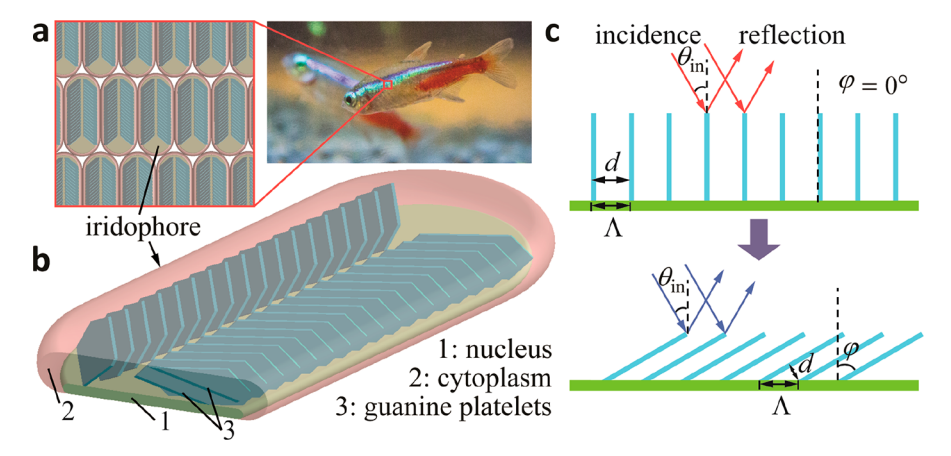


Figure 1. Schematic of neon tetra and its photonic structures. (a) Tropical fish neon tetra. The lateral stripe contains iridophore arrays. (b) Single iridophore. It consists of reflective guanine platelets, cytoplasm, and nucleus. (c) Schematic of "Venetian blind" mechanism of dynamic iridescence inspired by neon tetra.

cyanea), <sup>16</sup> where ordered multilayers in iridophore cells swell to change color. The panther chameleon (*Furcifer pardalis*)<sup>6</sup> can adjust the lattice constant of 3D guanine photonic nanocrystals by relaxing (or exciting) its skin, resulting in a strong blue (or red) shift. Using the accordion mechanism, magnetic tunable photonic structures have been demonstrated by colloidal nanocrystal clusters. <sup>17–22</sup> In addition to lattice changes, the refractive index can also be altered to adjust the optical wavelength within the medium, thereby shifting the interference condition. The beetle (*Charidotella egregia*)<sup>23</sup> is using this approach to modify the refractive index of each layer in a 1D Bragg mirror, switching the color from red to gold. Using the same mechanism, the beetle (*Hoplia coerulea*)<sup>2,4</sup> can modify color from blue to green.

In comparison, the tropical fish neon tetra (Paracheirodon innesi)4,5 uses a different mechanism for color change. In this approach, the structure orientation of a 1D periodic Bragg mirror stack is tilted by rotation about the base without changing lattice constant. This effectively reduces the gaps between the neighboring platelets about the facet normal, similar to a "Venetian blind".4 A detailed description of Venetian blind mechanism is described in Figure 1, where there are two lateral strips on neon tetra Paracheirodon innesi packed by iridophore cells (Figure 1a). Each iridophore cell contains two stacks of ordered parallel guanine platelets, a nucleus substrate, and cytoplasm that fills the space between platelets (Figure 1b). The alternating layers with high (guanine) and low (cytoplasm) refractive indces<sup>5</sup> form a multilayer reflector, contributing to peak reflection for the wavelength which is twice distance between the guanine platelets. With constant incident angle  $\theta_{\rm in}$  and lattice constant  $\Lambda$ , the platelets can be tilted with angle  $\varphi$  to change the perpendicular spacing between the platelets  $d = \Lambda \cos(\varphi)$ , thereby modifying the coloration (Figure 1c). However, it still has been less explored of artificial nanostructures or submicrostructures for tunable iridescence as specified by Venetian blind mechanism.

In this work, we introduce a strategy for dynamic iridescence by modifying the orientations of nanostructures according to the Venetian blind mechanism inspired by neon tetra. This approach is based on employing a 2D periodic magnetic nanopillar array as a template to guide the assembly of iron oxide nanoparticles in a liquid environment. Under an external magnetic field, the nanopillar array will generate a periodic local field to guide the self-assembly of iron oxide nanoparticles into periodic self-assembled columns (SACs). The local field generated also has an "anchor effect" and immobilizes the base of SACs, allowing them to be tilted about the base to induce color change. Using this method, the fabricated sample demonstrates dynamic iridescence with short response time around 0.3 s, high intensity tunability of up to 4-fold, and large peak wavelength shift of 190 nm in the visible range. The magnetically tunable material can be readily integrated on arbitrary surfaces to induce dynamic optical appearance.

The proposed Venetian blind mechanism has several advantages over the traditional accordion approach because the orientations of the photonic structures are modified without changing the lattice spacing. This can produce broader wavelength tuning range, which would require large strain using the accordion approach. In addition, the accordion approach generally requires the structure period to be similar to or smaller than the wavelength of visible light, such as those observed in colloidal particles with 100-155 nm diameter<sup>18-21</sup> and multilayer reflector with interbilayer distance between 66 and 250 nm. 25,26 However, such fine features increase fabrication demand and cost, especially for large areas. On the other hand, the peak reflection in Venetian blind approach is related to the normal distance  $d_i$ , which can be smaller than the lattice constant  $\Lambda$  with tilt angles. As a result, the structures with larger feature size ( $\Lambda \sim 2 \, \mu \text{m}$  in this work) can be used to achieve color change in the visible spectrum. In addition, spatially varying magnetic field profiles can be implemented using integrated microelectromagnet, 27,28 which can lead toward a programmable surface. Magnetic actuation also has low energy consumption, short response time, and high repeatability compared with other methods such as pH,<sup>29,30</sup> temperature,<sup>30–34</sup> electrochemical activation,<sup>25,34</sup> and mechanical force. 26,34 Tunable magnetic microstructures that imitate the Venetian blind mechanism have shown properties in microfluidics, <sup>35–42</sup> tunable wetting, <sup>43–45</sup> dry adhesion, <sup>46</sup> fog harvesting, <sup>47–49</sup> and light transmission. <sup>45,50</sup> Here we explore using this tilting mechanism to tune the reflectance spectra and color appearance in real time.

## **RESULTS AND DISCUSSION**

The fabrication of magnetic periodic template is implemented by using a combination of interference lithography and soft lithography (Figure 2a). Negative photoresist SU-8 and anti-

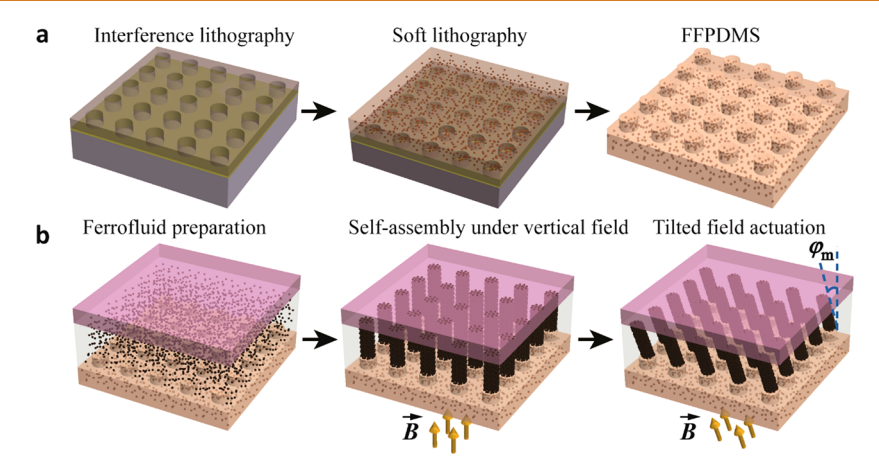


Figure 2. Fabrication processes. (a) Fabrication process of the FFPDMS template. A periodic SU-8 mold is fabricated by interference lithography. The FFPDMS precursor is then applied to the SU-8 mold, cured, and separated mechanically using soft lithography. (b) Self-assembly of nanoparticles in ferrofluid. Ferrofluid is applied on the FFPDMS template and sealed by a PDMS microfluidic channel. SACs can form and be tilted under vertical magnetic field and tilted field, respectively.

reflective coating (ARC) are first deposited onto a silicon substrate by spin-coating. The photoresist is then patterned using Lloyd's mirror interference lithography (IL)51,52 with a 325 nm wavelength laser to generate a 2D periodic array of circular holes. The pattern serves as a master for soft lithography molding the magnetic polymer material consisting of iron oxide nanoparticles (magnetite or Fe<sub>3</sub>O<sub>4</sub>, with diameter of 7-10 nm) and a copolymer of aminopropylmethylsiloxane (APMS) and dimethylsiloxane (DMS).53 The nanoparticles are bound with amine groups on the copolymer chains to establish a uniform ferrofluid complex, also called ferrofluid polydimethylsiloxane (FFPDMS). Details of material properties of FFPDMS are shown in Supporting Information, section A. After synthesis, the FFPDMS precursor fills into SU-8 master and is cured by formaldehyde vapor in vacuum environment. After separation, the cured FFPDMS yields in a 2D periodic array of magnetic nanopillars. More fabrication details are shown in Supporting Information, section B.

After the FFPDMS nanopillars array is prepared, it can serve as a template to direct the assembly of magnetic nanoparticles.<sup>54</sup> This process is illustrated in Figure 2b, where a polydimethylsiloxane (PDMS) microfluidic channel with 20 μm depth is prepared using standard microlithography methods to encapsulate the surface. It is introduced into the channel that a water-based ferrofluid composed of 0.125% (by volume) iron oxide nanoparticles with 10 nm diameter. The details of ferrofluid are shown in Supporting Information, section C. Under an out-of-plane external magnetic field, the iron oxide nanoparticles in the ferrofluid align to the field direction and assemble into SACs on top of the FFPDMS pillars. This increases the aspect ratio of the periodic assembled structure. At the same time, the SACs are anchored to the top of the nanopillar template, allowing the SAC to be rotated about its base. The template-directed SACs can be actuated and tilted to different angles.

The fabricated FFPDMS nanopillar array template is illustrated in Figure 3. The side-view scanning electron microscope (SEM) images over large area and high magnifications are shown in parts a and b of Figure 3, respectively. The top-view SEM image of the pillar is shown in Figure 3c. The FFPDMS nanopillars has a square lattice with period of 2  $\mu$ m. Each pillar is roughly 1  $\mu$ m in diameter and has a height-to-diameter aspect ratio of around 1. Note that there

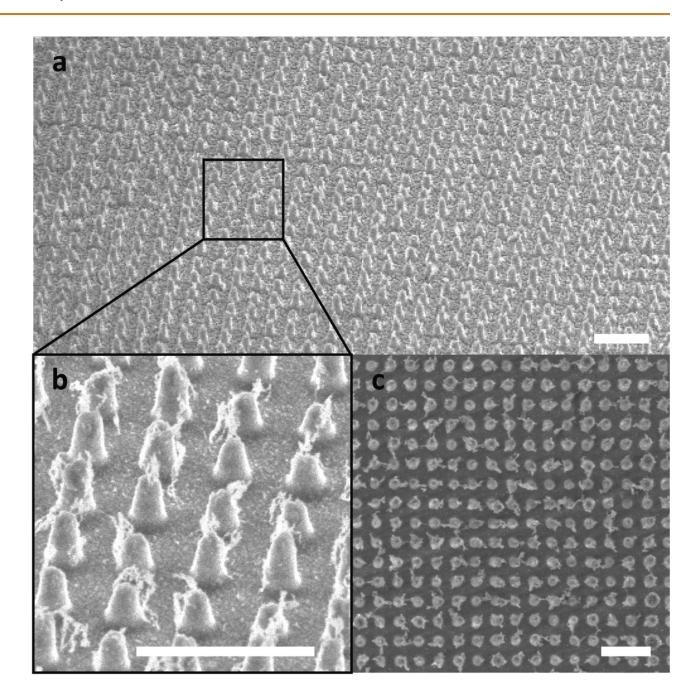


Figure 3. SEM images of FFPDMS template. (a,b) SEM images with 45° side view. (c) SEM image with top view. The scale bars in all images are 5  $\mu$ m. The surface roughness on the pillars can be due to polymer residue from the replication process.

is some surface roughness on the pillars, which can be attributed to polymer residue from the replication process. There is also a uniform residual layer of FFPDMS under the pillar structures with a thickness of approximately 20  $\mu$ m.

Characterization of Magnetic Tilt Actuation. The tilting behavior of the SACs on top of the FFPDMS nanopillar template is examined using top-view optical microscopy. A video of the magnetic actuation has been recorded (see Supporting Information, movie 1) and images corresponding to different magnetization conditions have been extracted and analyzed, as shown in Figure 4a. Initially, in the absence of an external magnetic field, the profile of the FFPDMS template is blurry because the nanoparticles in the ferrofluid are randomly distributed and scatter light. The top of one pillar is denoted by the white circle in the top-left image of Figure 4a. When an

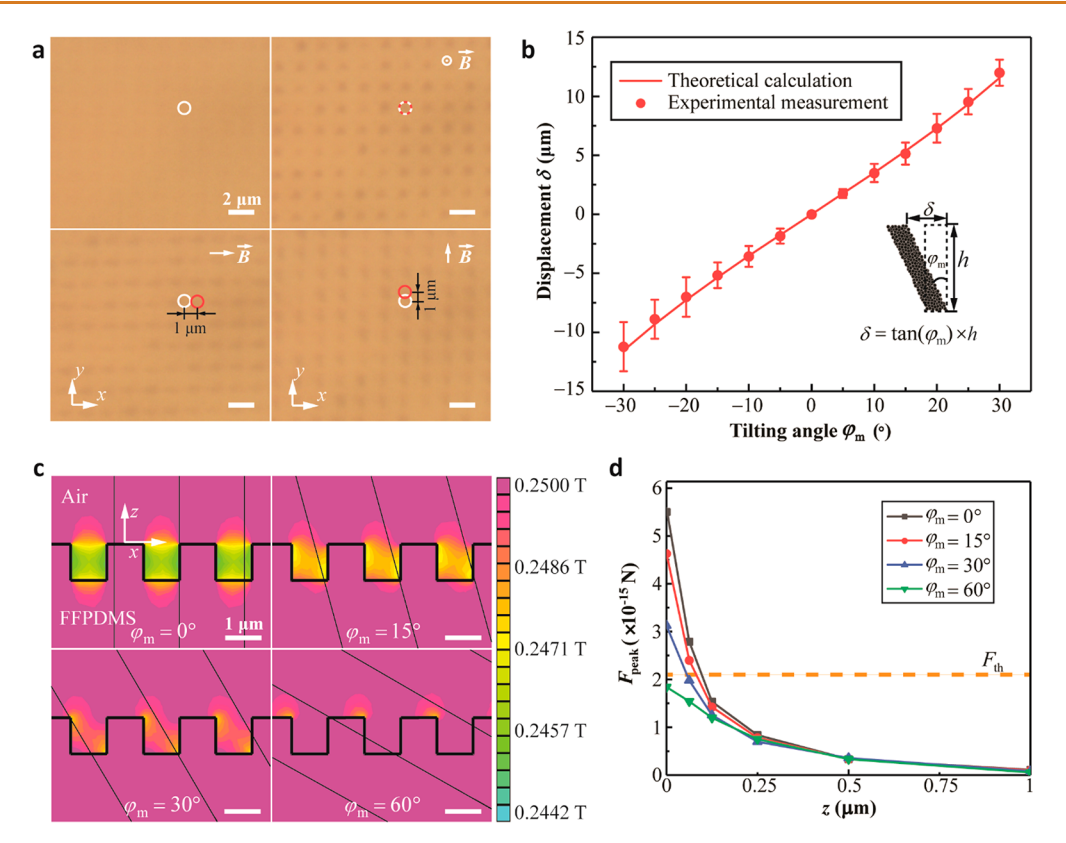


Figure 4. Tilt actuation characterization. (a) Microscopic images of ferrofluid with no field (top-left image), vertical field (top-right image), tilted field toward the positive x direction (bottom-left image), and tilted field toward the positive y direction (bottom-right image). The white circle indicates the original position of FFPDMS pillar and the red circle describes the deflected position of the SACs. The scale bars in images are 2  $\mu$ m. (b) The curve of the tilted displacement  $\delta$  of SACs and the tilt angle  $\varphi_{\rm m}$  of the external field, which is extracted by analyzing the microscopic images. It indicates that the SACs tend to align along the external field direction. Error bars represent the standard deviation in displacement. The SAC height h is 20  $\mu$ m. (c) Simulations of the local magnetic field on the FFPDMS pattern. The FFPDMS pillars are modeled as a rectangular grating with 2  $\mu$ m period, 1  $\mu$ m width, and 1  $\mu$ m height. The external field is 0.25 T, with the direction shown by black parallel lines in images. The scale bars in images are 1  $\mu$ m. (d) The comparison of the peak magnetic forces  $F_{\rm peak}$  at different tilt angles and the effective force of thermal fluctuation  $F_{\rm th}$ . When  $\varphi_{\rm m} \leq 30^{\circ}$  and  $z < 0.125 \,\mu$ m, the anchor effect can be maintained because  $F_{\rm peak} > F_{\rm th}$ .

out-of-plane external magnetic field is applied, the SACs form on top of the FFPDMS pillars and periodic patterns can be observed. The top of the SAC is denoted by the red circle, which overlaps with white circle, as shown in the top-right image of Figure 4a. When the external field is applied with angle  $\varphi_{\rm m}$  = 3° toward the positive x direction, as shown in the bottom-left image of Figure 4a, the tops of the SACs shift about 1  $\mu$ m toward the same direction. The displacement can be readily observed by the horizontal offset between the positions of the red and white circles, demonstrating that the SACs are tilted toward positive x direction. Similarly, when the external field is aligned at 3° toward the positive y direction, the tops of the SACs move about 1  $\mu$ m toward that direction, as shown in the bottom-right image of Figure 4a. More complex actuation maneuvers can be found in Supporting Information, movie 1, including rotation of the SACs in clockwise and counterclockwise directions. Once the field is removed, the SACs disperse back into water within 0.3 s. The transient response of the assembly is described in more details in Supporting Information, section D.

Further characterization of the relationship between the magnetic field angle  $\varphi_{\rm m}$  and the tilt actuation of SACs is summarized in Figure 4b. Assuming the top of SACs is confined by the microfluidic channel while the bottom is anchored on the FFPDMS pillars, as shown in the inset

schematic of Figure 4b, then the vertical height of SACs is constant at  $h = 20 \mu m$ . Thus, the displacement of the top of SACs is given by  $\delta = \tan(\varphi_m) \cdot h$ . The experimental data and theoretical model agree well, demonstrating that the SACs can be tilted along the external field direction. This also suggests the tilt actuation is a dynamic process that involves particle reorganization, which not only alters the orientation of the SACs but also elongates their length when compared with nontilted columns. The error bar for the data is calculated as the standard deviation of six independent measurements. At larger field angles,  $\varphi_{\rm m} > 30^{\circ}$ , the formation of the SACs have lower yield and further degrade. This can be attributed to two possible failure mechanisms: (1) the weakening of the anchor effect from the magnetic template, and (2) the degradation of assembly conditions, both of which will be discussed in more detail. As a result, the SACs cannot be systematically detected and are no longer periodic. Therefore, the dynamic range of the actuation angle tilt is limited to  $\pm 30^{\circ}$  in this work.

To investigate the underlying mechanism of tilted SACs, field-induced aggregation of magnetic nanoparticles in a fluid medium should be considered. When a thin layer of ferrofluid is confined by two parallel planes and subjected to out-of-plane magnetic field, the nanoparticles aggregate and form aligned chains along the field direction. SS-60 The vertical chains combine and form columns, resulting in the larger SACs. The

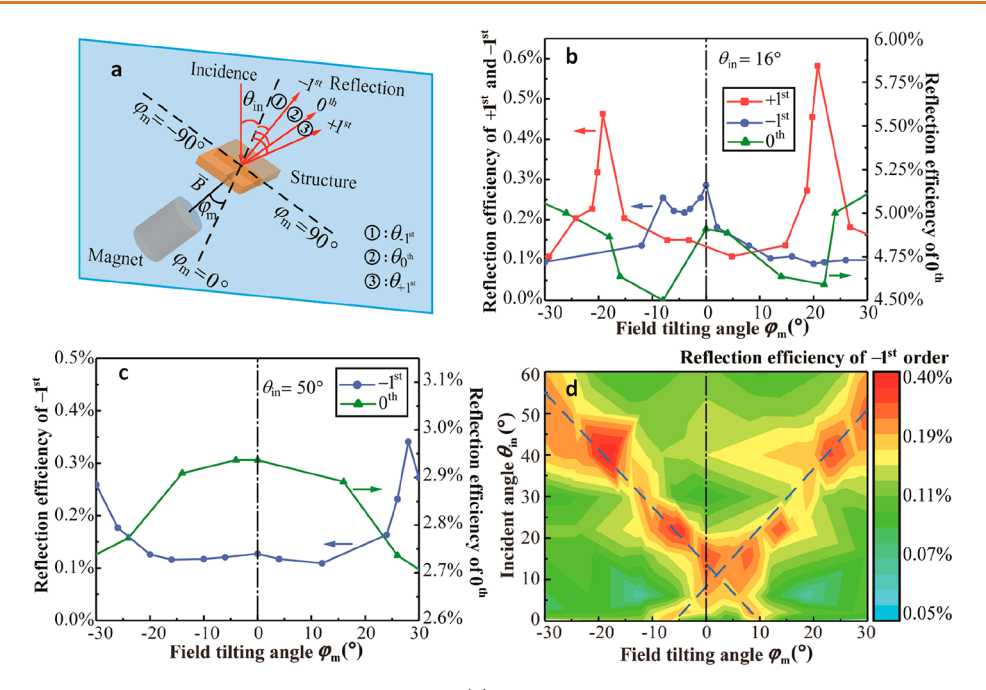


Figure 5. Reflection efficiency measurement with a 633 nm laser. (a) The schematic shows that there is reflection diffraction with various orders given an incident light beam with angle  $\theta_{\rm in}$ . The efficiency of the +1st, -1st, and 0th orders are measured under external magnetic field with tilt angle  $\varphi_{\rm m}$ . (b) Efficiency curves at  $\theta_{\rm in}$  = 16°. (c) Efficiency curves at  $\theta_{\rm in}$  = 50°. (d) 2D efficiency contour of the -1st order *versus* different incident angles and tilt angles.

formation of the SACs is a quasi-equilibrium process that involves the balance of magnetic energy, surface energy, and entropy. 55 From established theoretical models, 55,58 it can be observed that the particles require lower magnetic energy to assemble in channels with smaller confinement height. Therefore, when a periodic template is used instead of a flat plane, the particles tend to form columns first on the pillars rather than in the valleys. This can be attributed to the smaller confinement gaps h on the pillars, which results in less surface area and requires lower energy when the SACs form on the pillars as opposed to valleys. With an appropriate external field, the columns on pillars will repel each other to prevent other columns from existing in the valley, resulting in another configuration: a periodic rectangular pattern. In this case, the periodic template serves as a topography guide, and can be made by nonmagnetic material. However, nonmagnetic templates do not contribute to the anchoring of the SACs, which readily slips off when the magnetic field is applied at an angle.

To better interpret the anchor effect of the magnetic template and understand the failure mechanisms at large  $\varphi_{m}$ , simulations of the magnetic field profiles have been performed, as depicted in Figure 4c. The topography of FFPDMS pillars is modeled as a periodic rectangular grating with 2  $\mu$ m period, 1  $\mu$ m width, and 1  $\mu$ m height. The external magnetic field is set as 0.25 T. The color denotes magnetic flux density, while the black lines illustrate the field direction. When the external field is aligned vertically with tilt angle  $\varphi_{\rm m}$  = 0°, the color map shows that the FFPDMS pillars generate a periodic local field distribution. The magnetic flux density on the pillar tops is about 0.005 T higher than in the surrounding valleys, which induces a large field gradient of  $4 \times 10^4$  T/m. This creates a horizontal magnetic force attracting and trapping the base of the SAC, leading to the anchor effect. More details on the calculation of the magnetic force are described in Supporting Information, section E.

An estimate of the horizontal magnetic force can be calculated using the force equation<sup>61</sup>  $F = \nabla(m \cdot B)$ . The peak horizontal magnetic trapping force  $F_{\text{peak}}$  on a single nanoparticle is plotted as a function of the distance z away from the template, as shown in Figure 4d. The magnitude of the force is consistent with literature values observed in nanoparticle trapping.<sup>54</sup> For the particle to be trapped, the force has to overcome the effective force of thermal fluctuation  $F_{\rm th}$ , also shown in the figure. It can be observed that  $F_{\text{peak}} > F_{\text{th}}$  when z  $< 0.125 \ \mu \text{m}$  and  $\varphi_{\text{m}} \le 30^{\circ}$ , which indicates that trapping only occurs near the bottom of the SACs. Such an effect can overcome the random movements of SACs on a nonmagnetic template due to thermal fluctuation (Supporting Information, sections E and F, and Supporting Information, movies 1 and 2). However, at large z above the pillars, the field profile becomes more uniform, thus decreasing the attraction forces and allowing the upper parts of the SACs to move freely. When the external field is tilted at an angle, the periodic local field distribution will shift toward the field direction, as illustrated by the black solid parallel lines in Figure 4c. For  $\varphi_{\rm m} \leq 30^{\circ}$ , the magnetic force induced by the periodic template is still sufficient to trap particles to the base. As a result, the SACs will be aligned along the tilted external field direction while the base remains trapped on the templated FFPDMS pillars. If the tilt angle is too large, as shown in the case of  $\varphi_{\rm m}$  = 60°, the magnetic trapping force  $F_{\rm peak}$  <  $F_{\rm th}$  and the template will no longer anchor the SACs, leading to the first failure mechanism. This can be observed in the low anchoring yield for large  $\varphi_{m}$ , as shown in Supporting Information, section G. This model describes the mechanism of the magnetic anchor effect, which allows the rotation of the SACs about its base.

In addition to the weakening of the anchor effect, large  $\varphi_{\rm m}$  also leads to the degradation of the SAC assembly conditions, the second failure mechanism. This can be attributed to the non-normal confinement, which elongates the tilted SACs and increase their surface area. For such assemblies to be stable,

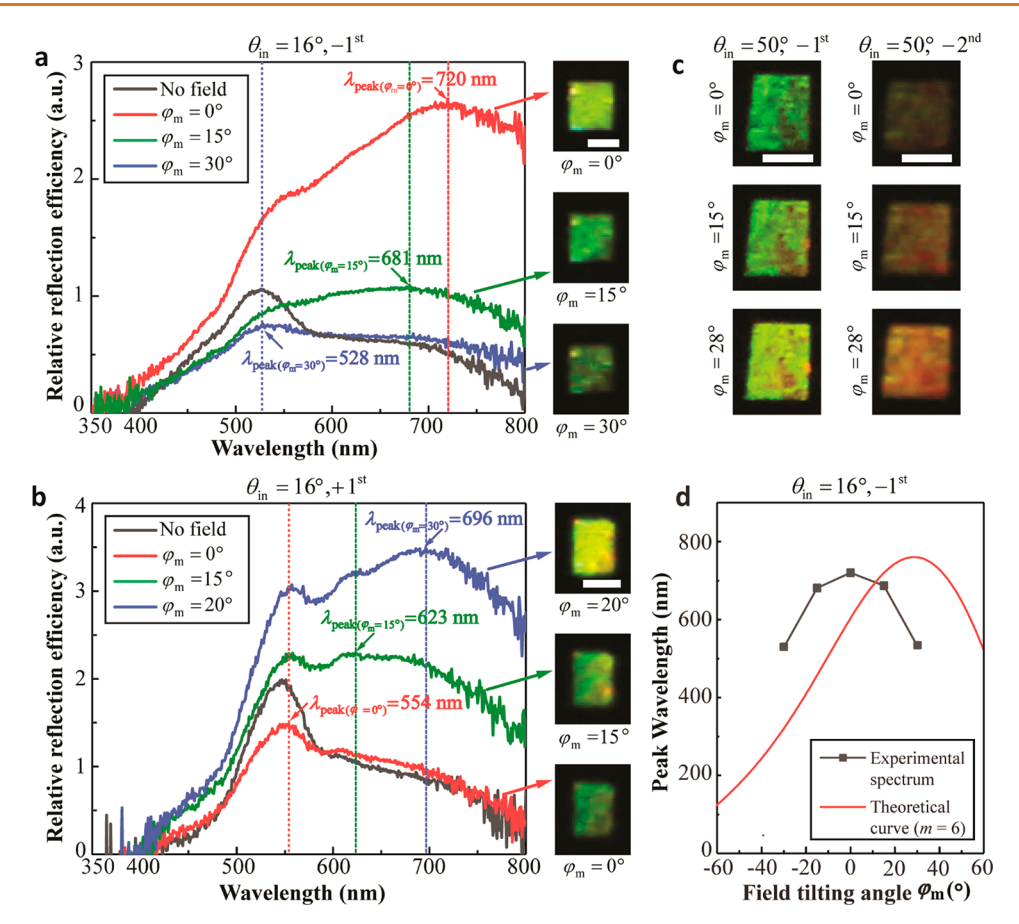


Figure 6. Iridescence demonstration using spectrometry measurement and camera images. (a) Spectra of the -1st order reflection diffraction at  $\theta_{\rm in}=16^{\circ}$  indicates a strong blue-shift, verified by camera images on the right side. The light source is white light. The scale bars in camera images are 1 mm. (b) Spectra of the +1st order reflection diffraction at  $\theta_{\rm in}=16^{\circ}$  indicates a strong red-shift and is demonstrated by camera images on the right side. The light source is white light. The scale bars in camera images are 1 mm. (c) Dynamic iridescence at  $\theta_{\rm in}=50^{\circ}$  for different orders. The left column shows a red-shift from green to yellow, the right column indicates a red-shift from indigo to orange. The scale bars are 1 mm. (d) The peak wavelength of the measured spectra for the -1st order and the theoretical curve using 1D multilayer reflector model

additional magnetic energy would have to be introduced, which is not the case in our system because the field magnitude is kept constant. This then leads to an imbalance of magnetic and surface energies, causing the assembly to degrade at large  $\varphi_{\rm m}$ . In this regime, the SACs tend to form longer, noncylindrical chains with large variations in diameter. The tilted permanent magnet can also induce a weak horizontal force through the in-plane field gradient, causing the SACs to continuously slide toward one direction. In addition, nonnormal magnetization can introduce a horizontal internal shear force on the SACs to further degrade the assembly. However, for small angles, the shear is small when compared to the out-of-plane component that drives the particle assembly. The degradation of the SACs at large  $\varphi_{\rm m}$  is discussed in more detail in Supporting Information, section G.

On the basis of the magnetic models that show poor trapping effect and the experimental observation that the particle assemblies are unstable and nonuniform for  $\varphi_{\rm m} > 30^{\circ}$ , the dynamic angle range of the tilt actuation is estimated to be  $-30^{\circ} \leq \varphi_{\rm m} \leq 30^{\circ}$  for this work. Even though some SACs can still form and be anchored at larger external field angles, the yield is low. In this regime, the tilted SACs are no longer periodic, which is an essential condition for structural coloration.

**Optical Characterization.** The fabricated prototype enables real-time control of the SACs tilt angle, which can trigger changes in optical properties. To demonstrate dynamic iridescence, the reflection efficiency of the fabricated device is characterized using a 633 nm laser. In this configuration, the light is incident on the structure at angle  $\theta_{\rm in}$  and induces different discrete diffraction orders based on Bragg's law, shown in the schematic in Figure 5a. A permanent magnet is installed on a rotational stage with the sample located at its center, hence the magnet can tilt with angle  $\varphi_{\rm m}$  at constant distance. The efficiencies of +1st, -1st, and 0th orders are measured with  $\theta_{\rm in}$  = 16° and TE polarization, as shown in Figure 5b. When  $\varphi_m$  increases from  $0^{\circ}$  to  $20^{\circ}$ , the efficiency of the +1st order (red curve) increases from 0.13% to a peak of 0.58%. This is conducive to a relative efficiency increase of roughly 4-fold. In contrast, the efficiency of the -1st order (blue curve) decreases from a peak of 0.29% to 0.12% when  $\varphi_{\mathrm{m}}$  increases from 0° to 20°, respectively. This indicates that +1st and -1st orders have opposite peak wavelength shifts and coloration effects when illuminated with white light source. On the other hand, the efficiency curve of the wavelengthindependent 0th order (green curve) does not vary between  $\varphi_{\rm m}$  = 0° and  $\varphi_{\rm m}$  = 30°. When the incident angle  $\theta_{\rm in}$  increases above 43°, the +1st order becomes evanescent according to Bragg's law, as shown in Supporting Information, section H.

For example, when the incident angle  $\theta_{\rm in}$  is 50°, the efficiency of the -1st order has a sharp peak of 0.34% at  $\varphi_{\rm m}=28^{\circ}$  with an efficiency increase of about 2-fold, while there is no +1st order, as shown in Figure 5c.

Considering the angular effects of the incident light and magnetic alignment, the efficiencies of the -1st order are plotted as a contour versus  $\theta_{\rm in}$  and  $\varphi_{\rm m}$ , as shown in Figure 5d. These results demonstrate that the reflection efficiency at 633 nm can be tuned from close to zero to 0.4%. This in turn generates different shades of red with changing magnetic alignment angle, demonstrating dynamic coloration and viewing angle dependence. It is interesting to notice that the efficiency of the -1st order is roughly symmetric with respect to the line  $\theta_{in} = 0^{\circ}$ . This can also be observed in the efficiency contour, where the peak efficiencies form symmetric lines and cross at about  $\varphi_{\rm m}$  = 5° (blue dashed lines of Figure 5d). This can be attributed to the variation of assembly quality with magnetization angle. When  $\varphi_m$  is nonzero, the magnetic field is not perpendicular to the physical confinement, inducing lower nanoparticles density packing. This effect is the same for tilt in both positive and negative direction, contributing to the efficiency symmetry. The efficiencies of the +1st and 0th orders are also symmetric and can be found in Supporting Information, section H.

The absolute reflection efficiencies of the structure are relatively low, which are attributed to the scattering and absorption of the residual FFPDMS layer. The reflection efficiency of silicon substrate is around 30%, and the absorption of FFPDMS residual layer is about 39%, which results in expected total reflection of 11.2%. The measured total efficiency for all orders is around 9%, which can be attributed to additional losses in the ferrofluid and PDMS microfluidic channel. The absolute efficiency can be improved by using a more reflective substrate, reducing the residual layer thickness and coating a thin reflective layer such as gold onto the FFPDMS template.

The structural coloration of the fabricated sample can be demonstrated by characterizing the reflectance spectra from 350 to 800 nm using a UV-vis-NIR spectrophotometer (Agilent Cary 5000). The details of the optical setup are shown in Supporting Information, section H. The measured spectra for the -1st and +1st orders at  $\theta_{in} = 16^{\circ}$  with different magnetic alignment angles  $\phi_{\rm m}$  = 0–30° are shown in Figure 6a,b. The visual appearance of the fabricated sample with a white light source at  $\theta_{\rm in}$  = 16° has been recorded using a camera with standard RGB color space, as shown in the inset diagrams. The real-time color tuning can be seen in Supporting Information, movies 3 and 4. As the field is tilted from  $\varphi_{\rm m} = 0^{\circ}$ to  $\varphi_{\rm m}$  = 30°, the color appearance of the -1st order can be varied from bright yellow to dark green, and the peak wavelength of the spectrum shifts from 720 to 528 nm, generating a blue-shift of 192 nm. This gives rise to a relative wavelength tunability  $\Delta \lambda/\lambda_0 = (\lambda_{\rm peak} - \lambda_0)/\lambda_0 = -26.7\%$ , where  $\lambda_0$  is the initial peak wavelength at  $\varphi_{\rm m} = 0^{\circ}$  and  $\lambda_{\rm peak}$  is the peak wavelength at  $\varphi_{\rm m}$  = 30°. The negative sign represents a blue-shift for the -1st order. On the contrary, the color appearance of the +1st order change from dark green to yellow with a red-shift when the field is tilted from  $0^{\circ}$  to  $20^{\circ}$ . The measured spectra indicate a red-shift of 142 nm, from 554 to 696 nm, with a tunability  $\Delta \lambda/\lambda_0 = +25.6\%$ . The comparisons of coloration and spectrum shifts for the +1st and -1st orders confirm our prediction of opposite behaviors in efficiency measurement in Figure 5b. In addition, the peak wavelength

shifts of –1st and +1st orders at negative tilt angles are similar to the shifts at positive tilt angles, as shown in Supporting Information, section H. The demonstrated peak wavelength shift is larger than those observed in organisms based on changes in index and strain, such as the beetle<sup>24</sup> (shift of 80 nm from 450 to 530 nm) and paradise whiptail<sup>15</sup> (shift of 185 nm from 465 to 650 nm), respectively. Most notably, the demonstrated peak wavelength shift is larger than those observed in the neon tetra<sup>4</sup> (shift of 90 nm from 400 to 490 nm), which is also based on the Venetian blind mechanism.

Beyond the shift of the peak wavelength, however, the measured spectra highlight a number of limitations for other optical properties. First, the overall reflection efficiency is low, which can be attributed to absorption and scattering of the FFPDMS as described previously. Second, it can be observed that the measured bandwidth in the reflectance spectra is relatively broad when compared with biological counterparts. It is therefore important to note that the perceived color does not correlative solely to the peak wavelength. For example, the peak wavelength of the +1st order at  $\varphi_{\rm m}$  = 15° is 623 nm, but the sample does not appear to be red. This can be attributed to another strong peak near 550 nm, which originates from the diffraction of the FFPDMS template, leading the perceived color to be yellowish green. Note at  $\varphi_{\rm m}$  = 20° the peak wavelength of the +1st order goes beyond the visible range to 720 nm, while the color of the sample appears yellow due to the secondary peak at green. The broad reflectance bandwidth can be due to the relatively short SACs lengths, resulting in fewer layers in the multilayer reflector. This is in contrast to the coherent reflection of stacked 1D platelets observed in neon tetra, which results in higher efficiency and narrower reflectance bandwidth. In addition, the SACs might also result in lower particle packing density during tilt actuation, which would induce lower index contrast with the liquid and further broaden the reflectance bandwidth. Increasing the height of the SACs can result in more structure periods along the light path for a more effective multilayer reflector and will be explored as potential solution to sharpen the reflectance bandwidth and increase reflection efficiency.

The color appearance is also dependent on incident and viewing angles, characteristic of iridescence. When the light incident angle is increased to  $\theta_{\rm in}=50^{\circ}$ , there is a red-shift from green to yellow as the field tilts from  $\phi_{\rm m}=0-30^{\circ}$ , as demonstrated in Figure 6c and Supporting Information, movie 5. Note this is also consistent with the efficiency measurement in Figure 5c. When the viewing angle is changed by about  $2^{\circ}$  and then kept fixed during the tilt actuation of SACs, the dynamic iridescence produces a broader red-shift from indigo to orange, as displayed in Supporting Information, movie 6. At even larger viewing angle of about  $8^{\circ}$ , it is possible to observe dynamic iridescence of the -2nd order, as shown in Figure 6c and Supporting Information, movie 7. The color appearance demonstrates a red-shift from green to orange, which is measured at a lower efficiency of about 0.1%.

To better understand the color shift mechanism, the peak wavelength  $\lambda_{\rm peak}$  can be plotted as a function of magnetization angle  $\varphi_{\rm m}$ , as shown in Figure 6d. On the basis of the Bragg reflector model, the peak wavelength can be calculated by constructive interference from alternating layers with high and low refractive indices corresponding to assembled nanoparticles and ambient water, respectively. The peak reflection occurs when the total normal distance between neighboring layers d is equal to an integer multiple m of a quarter of the

light wavelength. When the angle  $\varphi_{\rm m}$  varies, d changes to induce a shift in peak wavelength. The detailed derivation can be seen in Supporting Information, section H. Because the structure period of approximately 2  $\mu{\rm m}$  is used to affect visible light in this work, a higher order with m=6 is chosen for modeling. It can be deduced from Figure 6d that the peak wavelength of the  $-1{\rm st}$  order from spectra matches with the theoretical curve. Note the model predicts an asymmetric wavelength shift with respect to  $\varphi_{\rm m}$ , which was not replicated in the data due to degradation of particle assembly density at large  $\varphi_{\rm m}$ .

It should be recognized that the 1D multilayer Bragg reflector model is an approximation of the fabricated structures because both the magnetic template array and the SACs consist of 2D periodic structures. Further work is needed to provide a more comprehensive optical model of all different diffraction orders, as well as the bandwidth of the reflectance spectra. The proposed approach can also be implemented using 1D magnetic grating templates, which would result in nanoparticle assembly that more resemble platelets observed in neon tetra. The optical behavior of such structures would contain fewer diffraction orders and be better described by the Bragg model. However, the anchor effect in these structures would behave differently in the direction parallel to the template, which is the subject of ongoing work. One potential future work for the tunable 2D SACs is to analyze the behavior of dynamic iridescence under polarized light, which can lead to tunable birefringence and other polarization-dependent effect.

The proposed dynamic iridescence approach is enabled using a water-based ferrofluid within a microfluidic channel, and several considerations including sample reusability and water evaporation should be taken in account. The FFPDMS surface can be conveniently cleaned with a deionized water rinse due to the surface hydrophobicity to remove any nanoparticle residual, and therefore the FFPDMS template can be reused before becoming contaminated. However, one challenge is any water leakage leads to evaporation through the inlets and edges of the microfluidic channel, which currently limits the long-term durability of the device. The ability to achieve dry magnetic nanostructure with tunable tilt in ambient environment would be a more attractive alternative. However, this requires high aspect ratio FFPDMS nanostructures, which is a challenge to fabricate.

## **CONCLUSIONS**

We report an engineered nanostructured material with dynamic coloration and iridescence that can be magnetically tuned. This is based on a previously unexplored "Venetian blind" mechanism as inspired by the neon tetra, where the structure orientation is altered in real time to control the optical reflectance spectra. In this approach, the lithographically patterned FFPDMS pillar arrays function as an anchor for field-induced self-assembly of magnetic nanoparticles. This "anchor effect" enables the assembled columns to be tilted about the base, which changes the light interference condition. The fabricated structures demonstrated reversible color shifts from green to yellow with peak wavelength shift up to 192 nm. This approach offers potential applications for tunable magnetic structures as well as dynamic photonic devices by tilting the orientations of periodic structures. The proposed magnetic actuation can also be implemented using integrated electromagnets, which can lead to programmable iridescent display under ambient light. This active material

system can also find applications in dynamic camouflage coating, optical logical devices, microfluidics, and particle manipulation.

#### **METHODS**

Interference Lithography and Soft Lithography. First, ARC was spin-coated onto silicon wafer and baked at 90 °C for 1 min on a hot plate. Then SU-8 2002 was spin-coated onto the ARC and soft baked at 95 °C for 1 min on a hot plate. After exposure using Lloyd's mirror IL, the SU-8 sample was postexposure baked at 90 °C for 1 min on a hot plate, developed in PGMEA for 1 min, and rinsed with deionized water. FFPDMS precursor with 25 wt % of iron oxide nanoparticles was applied onto the SU-8 template in a desiccator with 15  $\mu$ L of formaldehyde, then the desiccator was pumped to -29 inHg vacuum for 6 h. After curing, the FFPDMS template was mechanically separated from SU-8 master. Ferrofluid (EMG 707, FerroTec) was confined on the FFPDMS using PDMS microfluidic channels fabricated by standard microlithography. For a magnetic field of 0.25 T, channel depth of 20  $\mu$ m, and particle volume fraction 0.125%, the SACs formed a rectangular periodic pattern on FFPDMS template with average spacing of 2  $\mu$ m. More details of materials and fabrication processes are shown in Supporting Information, sections

**Simulations and Software.** The magnetic field distribution contours in Figure 4c were simulated by the software FEMM. The magnetic properties of FFPDMS are described in more detail in Supporting Information, section A.

The displacement of SAC tops (the experimental curve of Figure 4b) was calculated by analyzing microscopy images using ImageJ. Magnetic forces were calculated using FEMM and Matlab.

**Dynamic Iridescence.** The structure and magnet are installed on user-customized rotation stage. The microscopy images and videos are taken by a Leitz Wetzlar microscope with  $1000\times$  magnification. A HeNe laser with  $\lambda=633$  nm was used as a light source to measure the efficiency of the FFPDMS and SACs. The efficiency data was collected using a silicon detector (918D-UV-OD3R, Newport). The spectrometry measurement was performed using UV-vis-NIR spectrophotometer (Cary 5000, Agilent). An optical system was used to achieve different incident and viewing angles, as shown in the schematic in Supporting Information, section H. The camera images and videos were taken by a Canon EOS 600D with standard RGB color space.

## **ASSOCIATED CONTENT**

## S Supporting Information

The Supporting Information is available free of charge on the ACS Publications website at DOI: 10.1021/acsnano.9b00822.

Additional information on magnetic and optical properties of FFPDMS, the behaviors of SACs under dynamic field, reflection efficiency measurements, spectrometry measurements (PDF)

Movie 1: The actuation characterization of SACs on the FFPDMS pattern using optical microscopy (AVI)

Movie 2: The actuation characterization of SACs on the PDMS pattern using optical microscopy (AVI)

Movie 3: The dynamic iridescence demonstration of the reflected -1st order at  $\theta_{\rm in}=16^{\circ}$ , which shows a blueshift (AVI)

Movie 4: The dynamic iridescence demonstration of the reflected +1st order at  $\theta_{in}$  = 16°, which shows a red-shift (AVI)

Movie 5: The dynamic iridescence demonstration of the reflected -1st order at  $\theta_{\rm in} = 50^{\circ}$  with an initial color of green, which shows a red-shift (AVI)

Movie 6: The dynamic iridescence demonstration of the reflected -1st order at  $\theta_{\rm in} = 50^{\circ}$  with an initial color of indigo, which shows a red-shift (AVI)

Movie 7: The dynamic iridescence demonstration of the reflected -2nd order at  $\theta_{\rm in}$  = 50°, which shows a redshift (AVI)

## **AUTHOR INFORMATION**

## **Corresponding Author**

\*E-mail: chichang@ncsu.edu.

# ORCID

Zhiren Luo: 0000-0001-6247-0196 Chih-Hao Chang: 0000-0003-4268-4108

## **Author Contributions**

C.-H.C. conceived the original idea and supervised the study. Z.L. performed the experiments, developed the models, and wrote the manuscript. B.E. synthesized the FFPDMS and provided guidance for the magnetic models. All the authors contributed to the paper revision and approved the finalized manuscript.

#### **Notes**

The authors declare no competing financial interest.

#### **ACKNOWLEDGMENTS**

We acknowledge X. Zhang at University of Pennsylvania for his help in interference lithography during his stay at North Carolina State University. This work was performed at the NCSU Nanofabrication Facility (NNF) and the Analytical Instrumentation Facility (AIF), members of the North Carolina Research Triangle Nanotechnology Network (RTNN), which is supported by the National Science Foundation as part of the National Nanotechnology Coordinated Infrastructure (NNCI). This work was supported by the Defense Advanced Research Projects Agency (DARPA) under grant W911NF-15-1-0108 and partially supported by National Science Foundation (NSF) grants CMMI#1552424 and MEP#1662641.

# **REFERENCES**

- (1) Isapour, G.; Lattuada, M. Bioinspired Stimuli-Responsive Color-Changing Systems. *Adv. Mater.* **2018**, *30*, 1707069.
- (2) Zi, J.; Yu, X.; Li, Y.; Hu, X.; Xu, C.; Wang, X.; Liu, X.; Fu, R. Coloration Strategies in Peacock Feathers. *Proc. Natl. Acad. Sci. U. S. A.* 2003, 100, 12576–12578.
- (3) Leclercq, E.; Taylor, J. F.; Migaud, H. Morphological Skin Colour Changes in Teleosts. Fish Fish 2010, 11, 159–193.
- (4) Gur, D.; Palmer, B. A.; Leshem, B.; Oron, D.; Fratzl, P.; Weiner, S.; Addadi, L. The Mechanism of Color Change in the Neon Tetra Fish: A Light-Induced Tunable Photonic Crystal Array. *Angew. Chem., Int. Ed.* **2015**, *54*, 12426–12430.
- (5) Yoshioka, S.; Matsuhana, B.; Tanaka, S.; Inouye, Y.; Oshima, N.; Kinoshita, S. Mechanism of Variable Structural Colour in the Neon Tetra: Quantitative Evaluation of the Venetian Blind Model. *J. R. Soc., Interface* **2011**, *8*, 56–66.
- (6) Teyssier, J.; Saenko, S. V.; van der Marel, D.; Milinkovitch, M. C. Photonic Crystals Cause Active Colour Change in Chameleons. *Nat. Commun.* **2015**, *6*, 6368.
- (7) Vukusic, P.; Sambles, J. R. Photonic Structures in Biology. *Nature* **2003**, 424, 852–855.
- (8) Prum, R. O.; Dufresne, E. R.; Quinn, T.; Waters, K. Development of Colour-Producing  $\beta$ -Keratin Nanostructures in Avian Feather Barbs. *J. R. Soc., Interface* **2009**, *6*, S253–S265.

- (9) Vukusic, P.; Sambles, J. R.; Lawrence, C. R.; Wootton, R. J. Quantified Interference and Diffraction in Single Morpho Butterfly Scales. *Proc. R. Soc. B* **1999**, *266*, 1403–1411.
- (10) Seago, A. E.; Brady, P.; Vigneron, J.-P.; Schultz, T. D. Gold Bugs and beyond: A Review of Iridescence and Structural Colour Mechanisms in Beetles (Coleoptera). *J. R. Soc., Interface* **2009**, *6*, S165–S184.
- (11) Sweeney, A.; Jiggins, C.; Johnsen, S. Insect Communication: Polarized Light as a Butterfly Mating Signal. *Nature* **2003**, 423, 31–32.
- (12) Land, M. F. The Physics and Biology of Animal Reflectors. *Prog. Biophys. Mol. Biol.* **1972**, 24, 75–106.
- (13) Fudouzi, H. Tunable Structural Color in Organisms and Photonic Materials for Design of Bioinspired Materials. *Sci. Technol. Adv. Mater.* **2011**, *12*, 064704.
- (14) Tao, A. R.; DeMartini, D. G.; Izumi, M.; Sweeney, A. M.; Holt, A. L.; Morse, D. E. The Role of Protein Assembly in Dynamically Tunable Bio-Optical Tissues. *Biomaterials* **2010**, *31*, 793–801.
- (15) Mäthger, L. M.; Land, M. F.; Siebeck, U. E.; Marshall, N. J. Rapid Colour Changes in Multilayer Reflecting Stripes in the Paradise Whiptail, Pentapodus Paradiseus. *J. Exp. Biol.* **2003**, *206*, 3607–3613.
- (16) Oshima, N.; Fujii, R. Motile Mechanism of Blue Damselfish (Chrysiptera Cyanea) Iridophores. *Cell Motil. Cytoskeleton* **1987**, 8, 85–90.
- (17) Kim, H.; Ge, J.; Kim, J.; Choi, S.; Lee, H.; Lee, H.; Park, W.; Yin, Y.; Kwon, S. Structural Colour Printing Using a Magnetically Tunable and Lithographically Fixable Photonic Crystal. *Nat. Photonics* **2009**, *3*, 534–540.
- (18) Luo, W.; Ma, H.; Mou, F.; Zhu, M.; Yan, J.; Guan, J. Steric-Repulsion-Based Magnetically Responsive Photonic Crystals. *Adv. Mater.* **2014**, *26*, 1058–1064.
- (19) Ge, J.; Goebl, J.; He, L.; Lu, Z.; Yin, Y. Rewritable Photonic Paper with Hygroscopic Salt Solution as Ink. *Adv. Mater.* **2009**, *21*, 4259–4264.
- (20) Hu, Y.; He, L.; Han, X.; Wang, M.; Yin, Y. Magnetically Responsive Photonic Films with High Tunability and Stability. *Nano Res.* **2015**, *8*, 611–620.
- (21) Shang, S.; Zhang, Q.; Wang, H.; Li, Y. Facile Fabrication of Magnetically Responsive PDMS Fiber for Camouflage. *J. Colloid Interface Sci.* **2016**, 483, 11–16.
- (22) Ge, J.; Yin, Y. Responsive Photonic Crystals. *Angew. Chem., Int. Ed.* **2011**, *50*, 1492–1522.
- (23) Vigneron, J. P.; Pasteels, J. M.; Windsor, D. M.; Vértesy, Z.; Rassart, M.; Seldrum, T.; Dumont, J.; Deparis, O.; Lousse, V.; Biró, L. P.; Ertz, D.; Welch, V. Switchable Reflector in the Panamanian Tortoise Beetle Charidotella Egregia (Chrysomelidae: Cassidinae). *Phys. Rev. E* **2007**, *76*, 031907.
- (24) Rassart, M.; Simonis, P.; Bay, A.; Deparis, O.; Vigneron, J. P. Scale Coloration Change Following Water Absorption in the Beetle Hoplia Coerulea (Coleoptera). *Phys. Rev. E* **2009**, *80*, 031910.
- (25) Walish, J. J.; Kang, Y.; Mickiewicz, R. A.; Thomas, E. L. Bioinspired Electrochemically Tunable Block Copolymer Full Color Pixels. *Adv. Mater.* **2009**, *21*, 3078–3081.
- (26) Yue, Y.; Kurokawa, T.; Haque, M. A.; Nakajima, T.; Nonoyama, T.; Li, X.; Kajiwara, I.; Gong, J. P. Mechano-Actuated Ultrafast Full-Colour Switching in Layered Photonic Hydrogels. *Nat. Commun.* **2014**, *5*, 4659.
- (27) Lee, C. S.; Lee, H.; Westervelt, R. M. Microelectromagnets for the Control of Magnetic Nanoparticles. *Appl. Phys. Lett.* **2001**, *79*, 3308–3310.
- (28) Deng, T.; Whitesides, G. M.; Radhakrishnan, M.; Zabow, G.; Prentiss, M. Manipulation of Magnetic Microbeads in Suspension Using Micromagnetic Systems Fabricated with Soft Lithography. *Appl. Phys. Lett.* **2001**, *78*, 1775–1777.
- (29) Zarzar, L. D.; Kim, P.; Aizenberg, J. Bio-Inspired Design of Submerged Hydrogel-Actuated Polymer Microstructures Operating in Response to PH. *Adv. Mater.* **2011**, 23, 1442–1446.
- (30) He, X.; Aizenberg, M.; Kuksenok, O.; Zarzar, L. D.; Shastri, A.; Balazs, A. C.; Aizenberg, J. Synthetic Homeostatic Materials with

Chemo-Mechano-Chemical Self-Regulation. *Nature* **2012**, 487, 214–218.

- (31) Wang, X.-Q.; Yang, S.; Wang, C.-F.; Chen, L.; Chen, S. Multifunctional Hydrogels with Temperature, Ion, and Magneto-caloric Stimuli-Responsive Performances. *Macromol. Rapid Commun.* **2016**, 37, 759–768.
- (32) Cui, J.; Drotlef, D.-M.; Larraza, I.; Fernández-Blázquez, J. P.; Boesel, L. F.; Ohm, C.; Mezger, M.; Zentel, R.; del Campo, A. Bioinspired Actuated Adhesive Patterns of Liquid Crystalline Elastomers. *Adv. Mater.* **2012**, *24*, 4601–4604.
- (33) Reddy, S.; Arzt, E.; del Campo, A. Bioinspired Surfaces with Switchable Adhesion. *Adv. Mater.* **2007**, *19*, 3833–3837.
- (34) Xu, C.; Stiubianu, G. T.; Gorodetsky, A. A. Adaptive Infrared-Reflecting Systems Inspired by Cephalopods. *Science* **2018**, 359, 1495–1500.
- (35) Evans, B. A.; Shields, A. R.; Carroll, R. L.; Washburn, S.; Falvo, M. R.; Superfine, R. Magnetically Actuated Nanorod Arrays as Biomimetic Cilia. *Nano Lett.* **2007**, *7*, 1428–1434.
- (36) Sniadecki, N. J.; Anguelouch, A.; Yang, M. T.; Lamb, C. M.; Liu, Z.; Kirschner, S. B.; Liu, Y.; Reich, D. H.; Chen, C. S. Magnetic Microposts as an Approach to Apply Forces to Living Cells. *Proc. Natl. Acad. Sci. U. S. A.* **2007**, *104*, 14553–14558.
- (37) Shields, A. R.; Fiser, B. L.; Evans, B. A.; Falvo, M. R.; Washburn, S.; Superfine, R. Biomimetic Cilia Arrays Generate Simultaneous Pumping and Mixing Regimes. *Proc. Natl. Acad. Sci. U. S. A.* **2010**, *107*, 15670–15675.
- (38) Fahrni, F.; Prins, M. W. J.; van IJzendoorn, L. J. Micro-Fluidic Actuation Using Magnetic Artificial Cilia. *Lab Chip* **2009**, *9*, 3413–3421.
- (39) Khademolhosseini, F.; Chiao, M. Fabrication and Patterning of Magnetic Polymer Micropillar Structures Using a Dry-Nanoparticle Embedding Technique. *J. Microelectromech. Syst.* **2013**, 22, 131–139.
- (40) Timonen, J. V. I.; Demirörs, A. F.; Grzybowski, B. A. Magnetofluidic Tweezing of Nonmagnetic Colloids. *Adv. Mater.* **2016**, 28, 3453–3459.
- (41) Khaderi, S. N.; Craus, C. B.; Hussong, J.; Schorr, N.; Belardi, J.; Westerweel, J.; Prucker, O.; Rühe, J.; den Toonder, J. M. J.; Onck, P. R. Magnetically-Actuated Artificial Cilia for Microfluidic Propulsion. *Lab Chip* **2011**, *11*, 2002–2010.
- (42) Toonder, J. den; Bos, F.; Broer, D.; Filippini, L.; Gillies, M.; de Goede, J.; Mol, T.; Reijme, M.; Talen, W.; Wilderbeek, H.; Khatavkar, V.; Anderson, P. Artificial Cilia for Active Micro-Fluidic Mixing. *Lab Chip* **2008**, *8*, 533–541.
- (43) Drotlef, D.-M.; Blümler, P.; Papadopoulos, P.; del Campo, A. Magnetically Actuated Micropatterns for Switchable Wettability. ACS Appl. Mater. Interfaces 2014, 6, 8702–8707.
- (44) Kim, J. H.; Kang, S. M.; Lee, B. J.; Ko, H.; Bae, W.-G.; Suh, K. Y.; Kwak, M. K.; Jeong, H. E. Remote Manipulation of Droplets on a Flexible Magnetically Responsive Film. *Sci. Rep.* **2016**, *5*, 17843.
- (45) Zhu, Y.; Antao, D. S.; Xiao, R.; Wang, E. N. Real-Time Manipulation with Magnetically Tunable Structures. *Adv. Mater.* **2014**, *26*, 6442–6446.
- (46) Drotlef, D.-M.; Blümler, P.; del Campo, A. Magnetically Actuated Patterns for Bioinspired Reversible Adhesion (Dry and Wet). *Adv. Mater.* **2014**, *26*, 775–779.
- (47) Peng, Y.; He, Y.; Yang, S.; Ben, S.; Cao, M.; Li, K.; Liu, K.; Jiang, L. Magnetically Induced Fog Harvesting *via* Flexible Conical Arrays. *Adv. Funct. Mater.* **2015**, 25, 5967–5971.
- (48) Huang, Y.; Stogin, B. B.; Sun, N.; Wang, J.; Yang, S.; Wong, T.-S. A Switchable Cross-Species Liquid Repellent Surface. *Adv. Mater.* **2017**, *29*, 1604641.
- (49) Cao, M.; Ju, J.; Li, K.; Dou, S.; Liu, K.; Jiang, L. Facile and Large-Scale Fabrication of a Cactus-Inspired Continuous Fog Collector. *Adv. Funct. Mater.* **2014**, *24*, 3235–3240.
- (50) Liu, S.; Long, Y.; Liu, C.; Chen, Z.; Song, K. Bioinspired Adaptive Microplate Arrays for Magnetically Tuned Optics. *Adv. Opt. Mater.* **2017**, *5*, 1601043.
- (51) Smith, H. I. Low Cost Nanolithography with Nanoaccuracy. *Phys. E (Amsterdam, Neth.)* **2001**, *11*, 104–109.

(52) Bagal, A.; Chang, C.-H. Fabrication of Subwavelength Periodic Nanostructures Using Liquid Immersion Lloyd's Mirror Interference Lithography. *Opt. Lett.* **2013**, *38*, 2531–2534.

- (53) Evans, B. A.; Fiser, B. L.; Prins, W. J.; Rapp, D. J.; Shields, A. R.; Glass, D. R.; Superfine, R. A Highly Tunable Silicone-Based Magnetic Elastomer with Nanoscale Homogeneity. *J. Magn. Magn. Mater.* **2012**, 324, 501–507.
- (54) Demirörs, A. F.; Pillai, P. P.; Kowalczyk, B.; Grzybowski, B. A. Colloidal Assembly Directed by Virtual Magnetic Moulds. *Nature* **2013**, *503*, 99–103.
- (55) Ytreberg, F. M.; McKay, S. R. Calculated Properties of Field-Induced Aggregates in Ferrofluids. *Phys. Rev. E: Stat. Phys., Plasmas, Fluids, Relat. Interdiscip. Top.* **2000**, *61*, 4107–4110.
- (56) Hong, C.-Y.; Jang, I. J.; Horng, H. E.; Hsu, C. J.; Yao, Y. D.; Yang, H. C. Ordered Structures in Fe3O4 Kerosene-Based Ferrofluids. J. Appl. Phys. (Melville, NY, U. S.) 1997, 81, 4275–4277.
- (57) Liu, J.; Lawrence, E. M.; Wu, A.; Ivey, M. L.; Flores, G. A.; Javier, K.; Bibette, J.; Richard, J. Field-Induced Structures in Ferrofluid Emulsions. *Phys. Rev. Lett.* **1995**, *74*, 2828–2831.
- (58) Richardi, J.; Ingert, D.; Pileni, M. P. Theoretical Study of the Field-Induced Pattern Formation in Magnetic Liquids. *Phys. Rev. E: Stat. Phys., Plasmas, Fluids, Relat. Interdiscip. Top.* **2002**, *66*, 046306.
- (59) Islam, M. F.; Lin, K. H.; Lacoste, D.; Lubensky, T. C.; Yodh, A. G. Field-Induced Structures in Miscible Ferrofluid Suspensions with and without Latex Spheres. *Phys. Rev. E: Stat. Phys., Plasmas, Fluids, Relat. Interdiscip. Top.* **2003**, *67*, 021402.
- (60) Wu, K. T.; Yao, Y. D.; Wang, C. R. C.; Chen, P. F.; Yeh, E. T. Magnetic Field Induced Optical Transmission Study in an Iron Nanoparticle Ferrofluid. *J. Appl. Phys.* (Melville, NY, U. S.) 1999, 85, 5959–5961.
- (61) Jackson, J. Classical Electrodynamics, 2nd ed.; Wiley: New York, 1975; pp 185.